Understanding Interfacial Photoswitching Mechanisms in Atomically-Thin TMD-Spiropyran Hybrids

Advanced Materials Technologies

ADVANCED MATERIALS TECHNOLOGIES
www.advmattechnol.com

RESEARCH ARTICLE OPEN ACCESS

Understanding Interfacial Photoswitching Mechanisms in Atomically-Thin TMD-Spiropyran Hybrids

Sewon Park[1] | Jaehoon Ji[1] | Michael Brophy[2] | John Audi[2] | Jean Rouillon[3] | Carlos Benitez-Martin[4] | Joakim Andréasson[3] | Jeong Ho You[2] | Jong Hyun Choi[1]

[1]School of Mechanical Engineering, Purdue University, West Lafayette, Indiana, USA | [2]Department of Mechanical Engineering, University of St. Thomas, St. Paul, Minnesota, USA | [3]Department of Chemistry and Chemical Engineering, Chalmers University of Technology, Gothenburg, Sweden | [4]Department of Chemistry and Molecular Biology, University of Gothenburg, Gothenburg, Sweden

Correspondence: Jong Hyun Choi (jchoi@purdue.edu)

Received: 8 December 2025 | **Revised:** 11 May 2026 | **Accepted:** 18 May 2026

Keywords: density functional theory | optoelectronics | photochromic molecules | photoisomerization | photoswitching | spiropyrans | Transition metal dichalcogenides | WS_2 | WSe_2

ABSTRACT

Photoresponsive molecular interfaces in two-dimensional (2D) semiconductors enable light-programmable control of electronic and optical properties. However, how molecular photoisomerization reshapes interfacial electronic structure remains unclear. Here we introduce an interfacial framework that elucidates how photoisomerization of surface-bound spiropyran (SP) modulates interfacial charge distribution via molecular-state-dependent electrostatic interactions, enabling reversible modulation of photoluminescence (PL) emission and electric conductivity. In SP-functionalized WSe_2 monolayers, visible light triggers formation of the closed-ring SP state that promotes nonradiative pathways and enhances current flow, whereas UV light converts it to the open-ring merocyanine (MC) form, restoring PL and conductivity. Density functional theory calculations with Bader charge and work function analyses reveal net charge variation of ~0.04 *e* per supercell and an accompanying work-function increase of approximately 0.16 eV, which may be responsible for the observed changes in PL and conductivity. Control experiments with WS_2-SP show negligible changes, confirming that light-induced modulation depends on intrinsic material properties and surface potential alignment. These findings define interfacial charge reorganization as the mechanism linking molecular photoisomerization to optoelectronic properties and provide design strategies for light-addressable 2D hybrid systems.

1 | Introduction

Two-dimensional (2D) transition metal dichalcogenides (TMDs) have emerged as promising semiconductors for both fundamental studies and advanced device technologies, owing to their atomically thin structures, strong light-matter interactions, and tunable electronic properties [1–3]. Each TMD layer consists of a transition-metal sheet sandwiched between two chalcogen layers, which can be isolated from a layered crystal by mechanical exfoliation [4]. This dimensional confinement results in tightly bound excitons, thickness-dependent indirect-to-direct bandgap transitions, and bandgaps spanning from visible to near-infrared region [5, 6]. TMDs combine high optical absorption, mechanical flexibility, and environmental stability, making them attractive for applications in photodetectors, light-emitting devices, and other optoelectronic systems [4, 7]. In the monolayer state, their direct bandgaps and strong photoluminescence (PL) provide a versatile platform to explore excitonic physics and light-driven processes [8]. These attributes also open opportunities to interface with photoresponsive molecules, enabling reversible, light-controlled modulation of interfacial states [9–11].

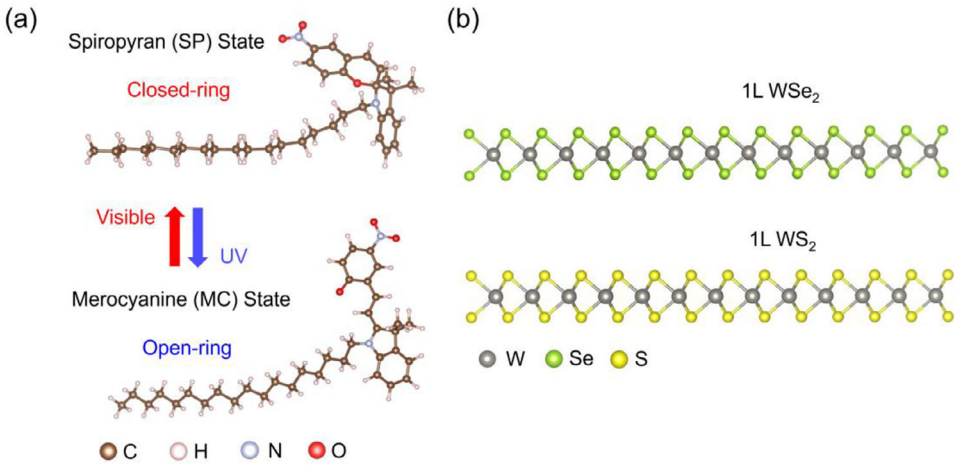

FIGURE 1 | Structural components and photoisomerization mechanism of the TMD-SP hybrid interface. (a) Reversible photoisomerization of the SP derivative between the closed-ring SP state and the open-ring MC state under visible UV and light irradiation, respectively. (b) Atomic structures of monolayer WSe_2 and WS_2. The integration of these molecular and TMD components forms a functional hybrid interface, where the molecular-state-dependent interactions between the isomers and the TMD lattices determine the overall optoelectronic response of the system.

The integration of photochromic molecules with 2D semiconductors offers a powerful route to achieve light-programmable optoelectronic responses. Photochromic molecules such as azobenzenes, diarylethenes, and spiropyrans (SP) can reversibly interconvert between isomers with distinct dipole moments and energy levels upon illumination with specific wavelengths [10, 12–14]. When interfaced with TMDs, these molecules can modulate carrier density, contact barriers, and excitonic recombination through changes in interfacial electrostatics or charge transfer [15, 16]. Previous studies have demonstrated photodoping and PL tuning in MoS_2 and $MoSe_2$ functionalized with azobenzene [17] or diarylethene derivatives [18–20], as well as humidity sensing and electrical switching in MoS_2-SP hybrids [21, 22]. The choice of molecules and 2D host determines the efficiency and reversibility of the modulation, as differences in band alignment, exciton binding energy, and dielectric screening govern the interfacial coupling [23–25].

Among TMDs, monolayer WSe_2 combines a direct bandgap in the visible range with intrinsic ambipolar transport and balanced electron-hole mobilities, making it uniquely suited for light-programmable interfaces [23, 26]. WSe_2 also exhibits strong optical absorption and pronounced PL, enabling molecular functionalization to modulate emission intensity and spectral position [27–29]. These properties create opportunities for recombination dynamics, multi-level optoelectronic responses, and enhanced design flexibility in molecularly functionalized devices [30, 31]. However, TMD/photochromic-layer research has so far been explored in only a limited set of material-molecule combinations, leaving vast opportunities for discovering new interfacial phenomena. Previous studies have provided valuable insights into interfacial modulation mechanisms, though the microscopic influence of molecular photoisomerization on local charge organization at atomically thin heterojunctions has been less explored. Establishing a monolayer WSe_2-SP platform therefore opens an unexplored avenue for stable, reversible, and wavelength-selective modulation in 2D optoelectronics, providing both a deeper fundamental understanding and a versatile design strategy for next-generation light-programmable devices.

In this work, we investigate photochromic-TMD hybrids functionalized with SP, which exhibit reversible modulation of optical and electrical responses under alternating visible and ultraviolet (UV) irradiation. Two TMDs with contrasting behaviors are studied under the same conditions, including WSe_2 and WS_2. PL and conductivity measurements reveal pronounced and reproducible switching in PL emission and electric conduction. We identify a new framework that explains this behavior based on density functional theory (DFT) calculations with Bader charge and work function analyses. The combined experimental and theoretical approach uncovers the fundamental connection between molecular configuration and local electronic potential, establishing a conceptual basis for light-controlled charge modulation in 2D hybrids.

2 | Results

2.1 | WSe_2-SP Hybrids

Figure 1a illustrates a SP molecule in its two photostable states. SP photoswitches reversibly interconvert between a closed-ring SP state and an open-ring MC state under alternating visible and UV illumination. In the SP state, the orthogonal C—O spiro linkage interrupts π-conjugation and maintains low polarity [32]. UV excitation drives an intramolecular charge-transfer process that weakens the spiro bond and induces ring opening. This transformation yields the planar MC state, characterized by extended π-delocalization and pronounced charge separation [14, 33]. Subsequent visible illumination promotes reverse isomerization to the SP state. This photoisomerization alters molecular dipole moment, switching between a weak, nearly perpendicular dipole in the SP state and a strong, in-plane dipole in the MC state. Such dipole reorientation modulates the local electrostatic potential, enabling optical control of interfacial charge redistribution when SP molecules are assembled on 2D semiconductors [10, 15, 34]. Under UV light (~312 nm), the molecules convert to the MC state, whereas visible irradiation (>530 nm) restores the SP state. Figure 1b displays the atomic arrangements of the monolayer

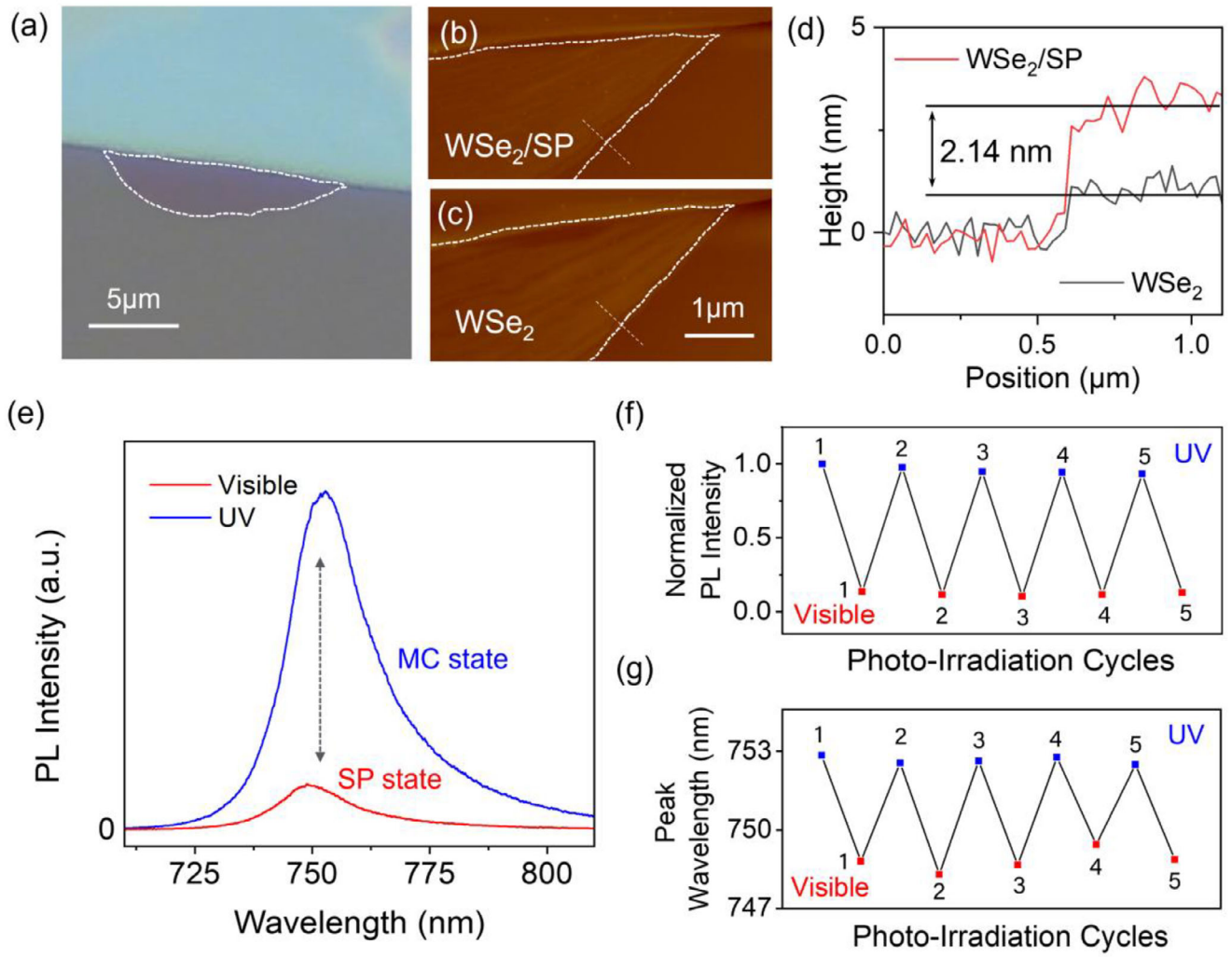

FIGURE 2 | (a) Bright-field image of a mechanically exfoliated monolayer WSe_2 flake on a SiO_2/Si substrate. (b) AFM image of the WSe_2-SP hybrid showing the formation of a continuous organic overlayer, compared with (c) pristine WSe_2. (d) Height profiles along the dashed lines in (b) and (c), yielding ~2.14 nm thickness for the SP molecular layer. (e) PL spectra under visible (red) and UV (blue) illumination at 633 nm excitation shows strong quenching in the SP state and recovery in the MC state. (f) Reversible switching of the PL intensity is observed over multiple irradiation cycles, demonstrating robust and reproducible photoswitching behavior at the hybrid interface. (g) The emission peak shows a reversible spectral shift between ~748 nm (SP state) and ~753 nm (MC state), confirming consistent wavelength tunability coupled to photoisomerization of the SP overlayer.

WSe_2 and WS_2 lattices, establishing the structural foundation for the material-dependent optoelectronic responses of the hybrid system.

The structural and optical properties of the WSe_2-SP hybrid were investigated by optical microscopy, atomic force microscopy (AFM), and PL spectroscopy (Figure 2). The optical image in Figure 2a highlights a monolayer WSe_2 flake, while the contrast between Figure 2b,c verifies the formation of uniform organic adlayer. This interfacial morphology reflects the dense and continuous nature of molecular assemblies on TMD surfaces and aligns with previously reported hybrid systems [35–38]. The corresponding height profile in Figure 2d shows a thickness of ~1.1 nm for bare monolayer WSe_2 and ~3.2 nm for the functionalized flake, giving an additional thickness of approximately 2.1 nm attributed to the SP layer. This height is consistent with a uniform, densely packed SP monolayer where the upright or slightly tilted orientation of the C18 alkyl chain contributes to the observed thickness [15]. In our experiment, the SP overlayer is consistent with a uniform thickness across many hybrids. These results confirm that the SP molecules form a uniform coating on the WSe_2 surface, providing a functionally integrated hybrid interface for subsequent studies.

The PL response of the hybrid reveals pronounced and reversible modulation upon photoisomerization. As shown in Figure 2e, the PL emission from WSe_2 is strongly quenched in the SP state. The quenched PL recovers when UV irradiation converts the molecules to the MC state. This change reflects efficient nonradiative quenching driven by interfacial electronic coupling between the WSe_2 and the SP state, while its suppression in the MC state restores radiative exciton recombination [39]. The reversibility of this effect is evident in Figure 2f, where alternating visible and UV illumination drives reproducible switching of the PL intensity over five consecutive cycles without any significant changes in the dynamic range (see Figures S3 and S4). Beyond intensity modulation, the PL spectra also display a systematic shift in peak position. Figure 2g shows that the emission maximum is

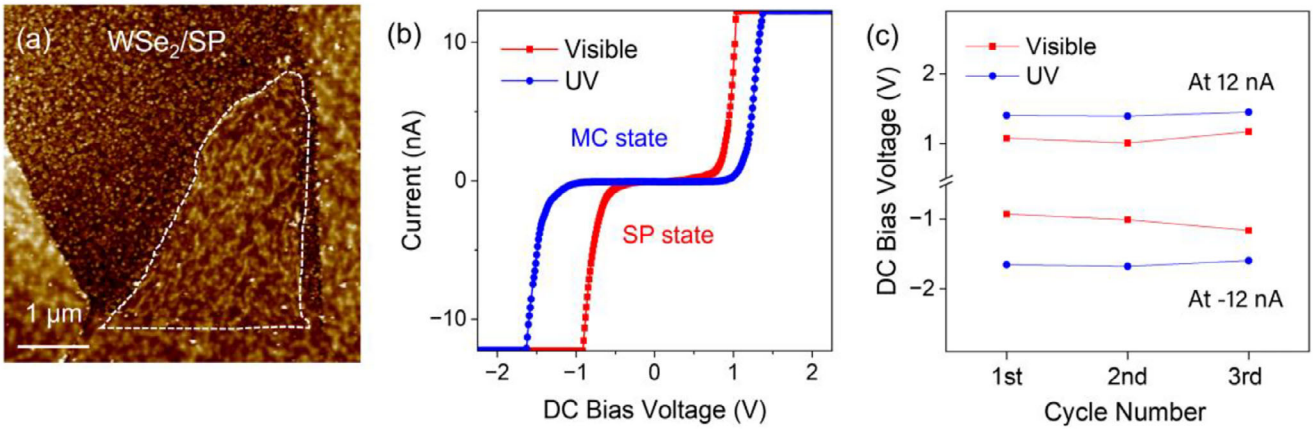

FIGURE 3 | (a) AFM image of a monolayer WSe_2 flake on an ITO substrate after SP functionalization. (b) I-V curves measured between −2 and +2 V with a current limit of ±12 nA, showing enhanced conduction in the SP state (visible light) and suppressed current in the MC state (UV light). (c) Bias voltages recorded at ±12 nA over three cycles demonstrate reversible and stable electrical switching under alternating illumination, highlighting the robustness and reproducibility of the optoelectronic response in the WSe_2-SP hybrid structure.

at approximately 753 nm in the MC state and shifts to ∼748 nm in the SP state. This ∼5 nm shift demonstrates that the optical response of WSe_2 can be modulated consistently by controlling the molecular configuration. These results demonstrate that the WSe_2-SP hybrid exhibits robust and reversible optical switching in which both the emission intensity and spectral position are governed by the molecular state [22].

The electrical properties of the WSe_2-SP hybrid were investigated using conductive AFM (C-AFM), as shown in Figure 3. The AFM topography on an ITO substrate shows that the monolayer flake remains intact after functionalization and exhibits a SP thickness of ∼2.2 nm confirms the formation of a uniform SP overlayer (Figures 3a). Current–voltage (*I–V*) measurements in Figure 3b show a strong dependence on the molecular configuration. In the SP state, the hybrid displays significantly higher current flow, whereas in the MC state generated under UV irradiation the current is lower across the same bias range. This modulation may be attributed to photoisomerization-induced variations in the interface. The observed current difference is consistent with light-induced changes in local charge redistribution, while molecular switching could also influence the tunneling barrier height and effective thickness, which together contribute to the overall modulation [10]. Figure 3c presents the reversibility of this modulation by showing the bias voltages at the ±12 nA limit, where three cycles of visible/UV switching produce alternation between high- and low-current states (also see Figures S5 and S6).

These electrical characteristics align with the optical response in Figure 2, where the PL intensity is quenched in the SP state and recovered in the MC state. The correlated *I–V* and PL behaviors demonstrate that photoisomerization induces light-controlled switching between these states, creating distinct interfacial electrostatic environments in WSe_2 that enable reproducible modulation of both emission and conduction [34, 40]. In the SP state, the molecular configuration establishes a highly localized interfacial electrostatic field (Figure S10), facilitating charge redistribution and opening additional nonradiative decay pathways that result in PL quenching [41, 42]. Upon switching to the MC state, spatially more delocalized dipole distribution relaxes the interfacial field, reducing carrier conduction while suppressing nonradiative losses and thereby recovering PL [32, 41].

2.2 | WS_2-SP Hybrids

We also examined WS_2 flakes functionalized with SP molecules. WS_2 monolayers with a thickness of ∼0.8 nm were prepared under the same conditions as WSe_2 and subsequently functionalized with SP molecules. AFM measurements confirmed an increase in thickness to ∼3.0 nm after functionalization, corresponding to an SP overlayer of ∼2.2 nm, nearly identical to that observed for the WSe_2-SP hybrid (Figure S7). The UV/visible irradiation conditions were also similar for photoisomerization in both systems. The PL measurement shows invariant spectra under visible and UV illumination (Figure 4a–c), and evaluations across multiple samples further confirm that both the emission intensity and peak wavelength remain nearly constant (Figure S8). It is thus evident that molecular photoisomerization does not significantly influence the emission characteristics of WS_2. Similarly, the *I–V* responses in Figure 4d remain essentially unchanged between the two molecular states, with the SP and MC configurations displaying overlapping *I–V* curves. These results, supported by consistent data from different flakes, clearly demonstrate that, in contrast to WSe_2-SP, the WS_2-SP hybrid does not exhibit light-controlled modulation in either optical emission or electrical conduction (Figure S9). This suggests that the molecular dipole reconfiguration does not sufficiently modify the electronic environment of WS_2. The microscopic origin of this material-dependent response is clarified in the following section through DFT analysis.

2.3 | DFT Analysis

To better understand the interfacial mechanisms at the atomic scale, we performed DFT calculations on both isolated SP and MC isomers and their hybrid structures with monolayer WSe_2 and WS_2. These calculations were designed to clarify how

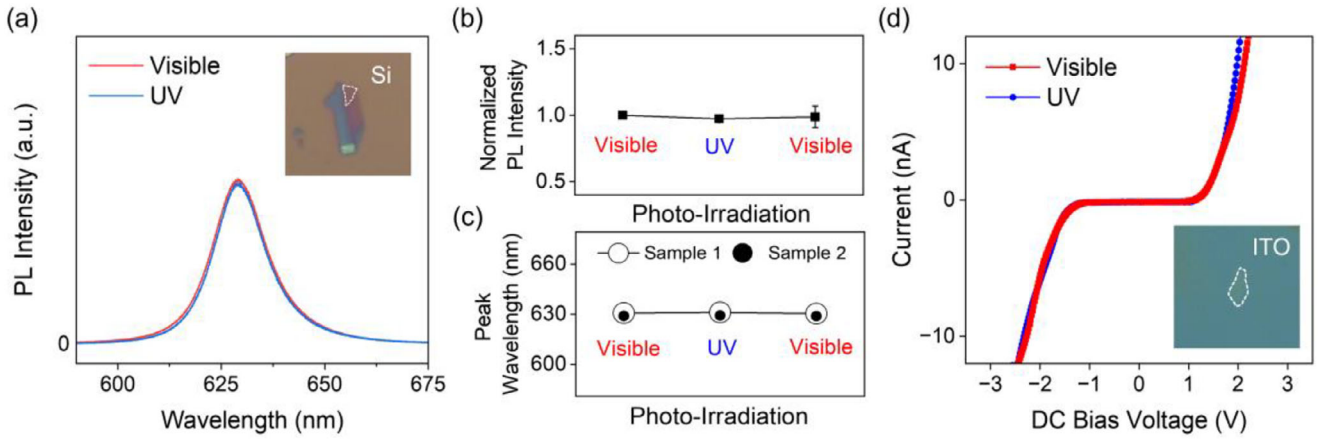

FIGURE 4 | Optical and electrical characterization of the WS_2-SP hybrid. (a) PL spectra of monolayer WS_2 after visible (red) and UV (blue) irradiation remain nearly identical in both intensity and peak position. The inset illustrates a bright-field image of a representative flake on a SiO_2/Si substrate. (b) Normalized PL intensity and (c) peak wavelength positions recorded over multiple photo-irradiations for different samples. The consistent data confirms the absence of switching behavior in the WS_2-SP system. (d) C-AFM measurement of *I–V* curves from −3 to +3 V with a ±12 nA limit, showing no significant differences between the SP and MC states. The inset presents a bright-field image of a flake on an ITO substrate.

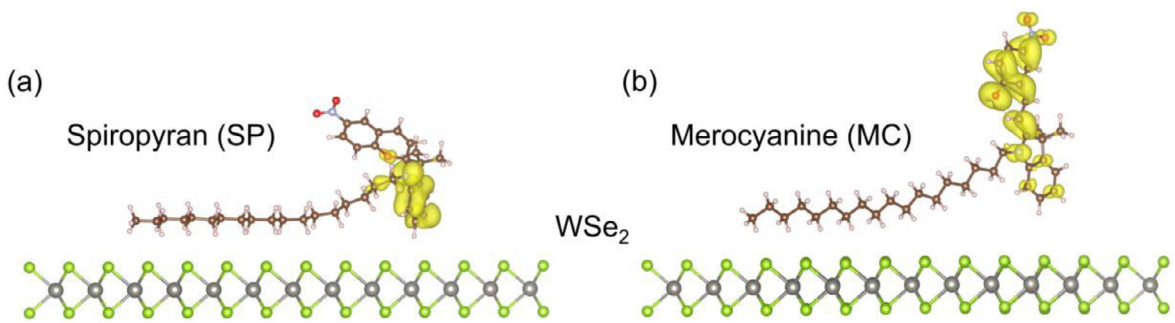

FIGURE 5 | DFT visualizations of electronic orbital distributions in SP and MC states on WSe_2 with charge density isosurface at 0.003 e/Å [3]. (a) HOMO of SP shows electron density localized close to the WSe_2 surface. (b) HOMO of MC extends further away from the surface. This proximity contrast is consistent with Bader charge analysis and indicates that isomerization produces a pronounced redistribution of interfacial electronic density in WSe_2.

molecular geometry, dipole orientation, and interfacial interactions influence charge redistribution and electronic coupling. We first optimized both SP and MC geometries on isolated molecules and then on TMD substrates to identify their preferred orientations and interfacial configurations. Within densely packed molecular assemblies, the dipole-down orientation of the SP state is energetically preferred by approximately 0.73 eV, reflecting stabilization through interactions between interfacial dipoles and the substrate (Figure S10). Upon UV irradiation, SP converts to the MC form, which retains the dipole-down configuration due to steric constraints in the closely packed adlayer. These optimized structures define the geometries used for subsequent interfacial analysis, as illustrated in Figure 5.

In the SP state, the highest occupied molecular orbital (HOMO) is compact and positioned close to the WSe_2 surface (Figure 5a), concentrating charge density near the closed-ring region and leading to a locally accumulated interfacial charge distribution [14]. In contrast, the HOMO of the MC state is redistributed over the delocalized π-system and displaced outward (Figure 5b), reducing overlap with the underlying TMD and weakening interfacial coupling. This relative proximity suggests that in the SP state, the molecule exerts a stronger local electrostatic influence on WSe_2, whereas in the MC state, the increased orbital delocalization mitigates this interfacial interaction. Figure S11 further highlights this distinction, with the SP HOMO and lowest unoccupied molecular orbital (LUMO) remaining spatially localized near the molecular core, while the MC orbitals are markedly delocalized. The stark contrast in orbital distributions between SP and MC states directly evidences how isomerization reorganizes interfacial charge density, generating distinct local electronic environments that account for the observed PL quenching and current modulation [43].

To understand the charge redistribution in the WSe_2-SP hybrid system, Bader charge analysis was performed on the isolated WSe_2 monolayer and the isolated molecule (Tables S1 and S2), as well as on the hybrid systems (Table S3). The Bader charge difference ($\Delta q = q_B^{\text{hybrid}} - q_B^{\text{isolated}}$, where q_B is the Bader charge) was calculated to quantify the interfacial charge redistribution between the molecule and the WSe_2 upon interaction. Overall, a redistribution magnitude of 0.070 e/supercell occurs between

WSe_2 and SP state, which is more than double the reorganization observed with MC state (0.031 *e*/supercell). The dominant PL quenching with the SP state is driven by the synergy between strong orbital proximity (~0.5 Å closer than MC) and a vertical dipole-down orientation that enhances interfacial dielectric screening, establishing a proximity-governed quenching regime. In contrast, the interfacial rearrangement of charge between the molecule and monolayer WS_2 is significantly reduced (0.019 *e*/supercell with SP and 0.001 *e*/supercell with MC).

The enhanced current response observed in the WSe_2 hybrid system with the SP state can be understood by examining the charge redistribution within the W-atom layer. In both WSe_2 and WS_2, the W-atom layer serves as the main conduction pathway due to the higher density of states (DOS) near the band edges (Figure S13). In the isolated WSe_2 monolayer, the W-atom layer possesses a Bader charge of 0.968 *e*/atom. Placing the SP-state molecule above the WSe_2 domain induces charge redistribution of 3.100 *e*/supercell (0.0775 *e*/atom) in the W-atom layer (Table S3). This redistribution amount significantly reduces to 2.657 *e*/supercell when the molecule converts to the MC state. The resulting charge difference of 0.443 *e*/supercell directly accounts for the pronounced I-V modulation observed in Figure 3b, which is primarily driven by localized interfacial charge redistribution within the W-atom layer. Conversely, the W-layer charge redistribution in the WS_2 hybrid system remains similar between the SP and MC states (Table S4), which is consistent with the *I–V* measurement shown in Figure 4b.

The net charge redistribution corresponds to approximately 0.011 *e*/W atom in WSe_2 but only about 0.001 *e*/W atom in WS_2, indicating that the interfacial perturbation experienced by the main conduction pathway is an order of magnitude larger in WSe_2. Although these per-atom variations are small in absolute terms, they are confined to the atomically thin W layer and are induced by a densely packed monolayer of photoswitchable dipoles at the interface. Modulations of this magnitude can act cooperatively across the interfacial dipole array, giving rise to large changes in the local carrier density and current [15, 44].

3 | Discussion

The DFT results are consistent with the experimentally observed changes and support the notion that photoisomerization reorganizes the interfacial charge density. The SP state exhibits strong interfacial coupling leading to PL quenching and enhanced current in WSe_2, while the MC state weakens this coupling, restoring PL and reducing conductance [20, 32, 33]. The optical and electrical modulations are primarily governed by interfacial electrostatics and localized charge redistribution. This microscopic redistribution of interfacial charge and dipole fields provides a plausible origin for the reversible PL spectral shift observed experimentally. Such a well-defined and repeatable modulation implies that the molecular dipoles are not randomly oriented but collectively organized at the interface [15]. It is important to note that the hydrophobic alkyl tail stabilizes this dipole alignment, maintaining a coherent interfacial field that alternates between strong and weak configurations in the SP and MC states, respectively [15, 45, 46]. In the SP state, the strong interfacial field enhances dielectric screening of the Coulomb interaction between electrons and holes in WSe_2, effectively weakening exciton binding and slightly raising the emission energy, which leads to quenched and blue-shifted PL [47, 48]. In the MC state, relaxation of the dipole field reduces this interfacial screening, restoring strong exciton binding and radiative recombination and thus resulting in a red-shifted and recovered PL emission [49].

The work function also tracks this dipolar reorganization, increasing from 5.22 eV in the SP state to 5.38 eV in the MC state for WSe_2 and from 5.23 to 5.50 eV for WS_2. While these work-function shifts are similar, a sizable shift alone does not guarantee marked switching in optical or electrical responses, as its effectiveness depends on interfacial electrostatic interactions. To elucidate this material dependence, we compared the intrinsic electronic structures of WSe_2 and WS_2. Our DOS calculations yield bandgaps of ~1.5 eV for monolayer WSe_2 and ~1.9 eV for WS_2, consistent with other reports [50]. WSe_2 exhibits a relatively small intrinsic bandgap and weakly bound excitons that are highly sensitive to even modest variations in the surrounding electrostatic environment [51–53]. As a result, molecular isomerization at the interface can efficiently reshape exciton formation and carrier distribution, producing measurable modulation of both PL and current.

In contrast, WS_2 features more strongly bound excitons that are less responsive to variations in the surrounding electrostatic environment [54, 55], showing limited response to comparable interfacial electrostatic variation [56]. Although a comparable work-function increase of +0.27 eV is observed upon MC formation, no considerable modulation of PL or conduction occurs. This contrast shows that the magnitude of the work-function change alone cannot account for the photoswitching efficiency, as it primarily reflects how effectively the interfacial electrostatic perturbation influences the material's electronic and excitonic states [57]. Furthermore, our DOS calculations reveal that both WSe_2 and WS_2 form similar hole-transfer-dominant heterojunctions with the isomers (Figure S14). This confirms that the band alignment alone cannot account for the drastically different photoswitching behaviors [12, 44].

This material dependence is further supported by the orbital-resolved DOS, which shows that the chalcogen p states in WS_2 span a broader energy range near the band edge, whereas those in WSe_2 are concentrated within a narrower window (Figure S15). The broader distribution in WS_2 offers fewer energetically favorable pathways for interfacial charge rearrangement, limiting the ability of its electron density to respond to electrostatic changes. By contrast, the more focused p-state distribution in WSe_2 enables charge redistribution to occur more efficiently, rendering its electronic structure more sensitive to variations in the interfacial electrostatic environment. This behavior is consistent with the reduced Bader charge variation obtained for WS2 [50, 58]. Efficient photoswitching in TMD-SP hybrids therefore requires both substantial reorganization of interfacial electrostatics and a host material whose electronic structure allows effective coupling between the interfacial electrostatic field and excitonic states [59]. In addition, highly responsive excitonic landscape in the host is essential for translating molecular-state-dependent charge redistribution into measurable optoelectronic responses.

4 | Conclusion

This work shows that WSe_2 functionalized with a uniform photochromic molecular layer exhibits robust and reversible photoswitching in both optical and electrical channels, while WS_2 monolayers remain unresponsive between SP and MC states. In monolayer WSe_2, the SP state quenches PL and enhances current flow, whereas the MC state restores emission intensity and reduces conduction. These results are consistent with DFT and Bader charge analysis, which reveal that molecular isomerization reorganizes interfacial electronic density and dipole orientation, producing distinct surface electronic environments. The contrasting responses of WSe_2 and WS_2 establish that material-dependent modulation is a decisive factor for achieving efficient photoswitching in TMDs.

The findings from this study establish a new conceptual framework for hybrid molecular-semiconductor interfaces, where photoisomerization drives interfacial electron-density redistribution that directly links molecular configuration to local electronic potential. Building on this concept, the design of hybrids requires collective control of multiple factors, including molecular dipole strength, interfacial organization, and substrate polarizability, which together dictate the magnitude and reversibility of optical and electronic modulation. Within this framework, the molecular architecture, including the alkyl tail that promotes ordered assembly and interfacial stability, illustrates how structural design can reinforce cooperative photoisomerization and ensure reproducible switching behavior.

WSe_2-SP hybrids thus represent a promising platform for light-programmable 2D interfaces, offering mechanistic insight and practical guidance for hybrid optoelectronics. By coupling molecular reconfiguration with the excitonic and transport properties of WSe_2, this work demonstrates a viable route to control emission and conduction without external gating. The observed stability and reproducibility indicate potential applications in ultrathin photodetectors, optical memories, neuromorphic circuits, and reconfigurable sensing elements, where molecular states act as addressable units. Further integration with heterostructures or flexible support could broaden the design space and facilitate new device architectures. More broadly, this study suggests that molecular functionalization provides an effective means to tune the electronic and optical behavior of 2D materials, pointing toward emerging opportunities in programmable optoelectronics at the molecular level [60, 61].

5 | Materials and Methods

5.1 | Preparation of Wse_2 and Ws_2

Monolayer WSe_2 and WS_2 flakes were mechanically exfoliated from bulk crystals (2D Semiconductors) using the conventional Scotch tape method and transferred onto cleaned p-doped SiO_2/Si substrates and ITO glass substrates (MTI KJ Group) [62, 63]. Prior to exfoliation, SiO_2/Si substrates were thoroughly cleaned by sequential ultrasonication in acetone, methanol, and deionized water for 15 min each to remove organic or particulate contaminants [64]. After cleaning, the substrates were dried using compressed air and soft-baked on a hot plate at 110°C for 5 min to ensure complete evaporation of residual solvents. To improve adhesion between the exfoliated flakes and the substrates, the samples were heated on a hot plate at 50°C after exfoliation. The heating duration was 10 min for SiO_2/Si substrates and 30 min for ITO substrates to enhance flake-substrate contact. After tape removal, all samples were annealed in an argon atmosphere at 250°C for 1 h to reduce interfacial contamination and improve interface quality.

5.2 | Synthesis of the Spiropyran (SP) Derivative

Experimental procedures for the synthesis and characterization of the SP derivative are detailed in the Supporting Information.

5.3 | Molecular Functionalization of WSe_2 and WS_2 Monolayers

Exfoliated WSe_2 and WS_2 flakes deposited on SiO_2/Si and ITO substrates were immersed in a 1 mM SP solution in ethanol for 12 h at 4°C to enable uniform surface adsorption [34]. After incubation, excess solution was removed by blowing compressed air, followed by soft baking at 50°C for 30 min to enhance molecular adhesion. To prevent unintentional photoisomerization, all treated samples were stored in a dark environment prior to optical switching. For SP to MC conversion, UV irradiation was performed using a Spectroline TE lamp (~2 mW/cm^2, 312 nm) for 2 min. Reversion to the SP state was achieved by exposure to visible light using a Xe-arc lamp equipped with a long-pass filter (>530 nm) for 20 min. These wavelengths were selected to align with the absorption range of the SP (~312 nm) and MC (~600 nm) states, ensuring selective photoisomerization [15]. The light intensity during visible irradiation was approximately 8 mW/cm^2, as measured with a calibrated power meter (Newport). The low power density was used to remain well below the damage thresholds of monolayer TMDs, thereby minimizing potential photothermal contributions and ensuring fatigue resistance [65].

5.4 | Sample Characterization

The PL measurements were conducted using a Renishaw inVia confocal Raman microscope under ambient conditions. Monolayer WSe_2 and WS_2 flakes were identified with a CCD camera and examined using various objective lenses (10×, 20×, 50×, and 100×) [66]. PL spectra were collected using a 633 nm HeNe laser for WSe_2 and a 532 nm diode-pumped solid-state laser for WS_2, with excitation wavelengths chosen to minimize overlap with SP absorption [15]. A 100× objective lens was used for PL collection to achieve a tightly focused beam with a spot size of approximately 1 μm2. Morphological and electrical properties were examined using AFM (Bruker Dimension Icon) equipped with SCANASYST-AIR probes for topographical imaging and SCM-PIT-V2 Pt/Ir-coated conductive probes for C-AFM measurements. Flake thicknesses were determined by height profile analysis under tapping mode. C-AFM was employed to evaluate local current distribution in both pristine and SP-treated samples. A bias voltage ranging from −2 to +2 V was applied with a current limit of ±12 nA and sensitivity of 1 nA/V to avoid tip or

sample damage [29]. All topographic and electrical measurements were performed on SiO_2/Si and ITO substrates under ambient conditions.

5.5 | Computational Methods

DFT calculations were carried out with the projector augmented wave method using Vienna Ab initio Simulation Package (VASP) [67–69]. Electron exchange and correlation were handled with the Perdew-Burke-Ernzerhof (PBE) functional within the generalized gradient approximation [70]. The SP/MC molecule was positioned on top of the TMD monolayer in a dipole-down orientation, and a vacuum spacing of at least 15 Å was introduced to avoid interlayer interactions. The corresponding areal density is 2.59×10^{13} and 2.83×10^{13} molecules/cm^2 for WSe_2 and WS_2, respectively. To describe the van der Waals interactions between the molecule and the TMDs, a dispersion correction was incorporated using the DFT-D2 method with Grimme [71]. A net dipole moment correction was added in a direction perpendicular to the monolayer. The electronic minimization was performed with a tolerance level of 10^{-5} eV. Ionic positions were relaxed until the Hellmann-Feynman forces were below 10 meV/Å with a $2 \times 4 \times 1$ Γ-centered **k**-point mesh for the molecule-(10×4) TMD hybrid systems. After the ionic relaxation, a finer **k**-point mesh of $3 \times 6 \times 1$ Γ-centered mesh was used for electronic property calculations.

Acknowledgements

This work was funded by the U.S. National Science Foundation under award nos. 2151869 and 2151887.

Conflicts of Interest

The authors declare no conflicts of interest.

Data Availability Statement

The data that support the findings of this study are available from the corresponding author upon reasonable request.

References

1. K. S. Novoselov, A. Mishchenko, A. Carvalho, and A. Castro Neto, "2D materials and van der Waals Heterostructures," *Science* 353, no. 6298 (2016): aac9439, https://doi.org/10.1126/science.aac9439.

2. K. F. Mak and J. Shan, "Photonics and Optoelectronics of 2D Semiconductor Transition Metal Dichalcogenides," *Nature Photonics* 10, no. 4 (2016): 216–226, https://doi.org/10.1038/nphoton.2015.282.

3. H. Wang, H. Yuan, S. S. Hong, Y. Li, and Y. Cui, "Physical and Chemical Tuning of Two-Dimensional Transition Metal Dichalcogenides," *Chemical Society Reviews* 44, no. 9 (2015): 2664–2680, https://doi.org/10.1039/C4CS00287C.

4. Q. H. Wang, K. Kalantar-Zadeh, A. Kis, J. N. Coleman, and M. S. Strano, "Electronics and Optoelectronics of Two-dimensional Transition Metal Dichalcogenides," *Nature Nanotechnology* 7, no. 11 (2012): 699–712, https://doi.org/10.1038/nnano.2012.193.

5. A. Splendiani, L. Sun, Y. Zhang, et al., "Emerging Photoluminescence in Monolayer MoS_2," *Nano Letters* 10, no. 4 (2010): 1271–1275, https://doi.org/10.1021/nl903868w.

6. S. Manzeli, D. Ovchinnikov, D. Pasquier, O. V. Yazyev, and A. Kis, "2D transition Metal Dichalcogenides," *Nature Reviews Materials* 2, no. 8 (2017): 17033.

7. M. Chhowalla, Z. Liu, and H. Zhang, "Two-Dimensional Transition Metal Dichalcogenide (TMD) Nanosheets," *Chemical Society Reviews* 44, no. 9 (2015): 2584–2586, https://doi.org/10.1039/C5CS90037A.

8. K. F. Mak, C. Lee, J. Hone, J. Shan, and T. F. Heinz, "Atomically Thin MoS_2: A New Direct-Gap Semiconductor," *Physical Review Letters* 105, no. 13 (2010): 136805, https://doi.org/10.1103/PhysRevLett.105.136805.

9. A. S. Pawbake, R. G. Waykar, D. J. Late, and S. R. Jadkar, "Highly Transparent Wafer-Scale Synthesis of Crystalline WS_2 Nanoparticle Thin Film for Photodetector and Humidity-Sensing Applications," *ACS Applied Materials & Interfaces* 8, no. 5 (2016): 3359–3365, https://doi.org/10.1021/acsami.5b11325.

10. Y. Zhao, S. Ippolito, and P. Samorì, "Functionalization of 2D Materials with Photosensitive Molecules: From Light-Responsive Hybrid Systems to Multifunctional Devices," *Advanced Optical Materials* 7, no. 16 (2019): 1900286, https://doi.org/10.1002/adom.201900286.

11. S. Bertolazzi, M. Gobbi, Y. Zhao, C. Backes, and P. Samorì, "Molecular Chemistry Approaches for Tuning the Properties of Two-Dimensional Transition Metal Dichalcogenides," *Chemical Society Reviews* 47, no. 17 (2018): 6845–6888, https://doi.org/10.1039/C8CS00169C.

12. Y. Zhao, S. Bertolazzi, and P. Samorì, "A Universal Approach toward Light-Responsive Two-Dimensional Electronics: Chemically Tailored Hybrid van der Waals Heterostructures," *ACS Nano* 13, no. 4 (2019): 4814–4825, https://doi.org/10.1021/acsnano.9b01716.

13. J. Andersson, S. Li, P. Lincoln, and J. Andréasson, "Photoswitched DNA-Binding of a Photochromic Spiropyran," *Journal of the American Chemical Society* 130, no. 36 (2008): 11836–11837, https://doi.org/10.1021/ja801968f.

14. C. L. Fleming, S. Li, M. Grøtli, and J. Andréasson, "Shining New Light on the Spiropyran Photoswitch: a Photocage Decides between Cis—Trans or Spiro-Merocyanine Isomerization," *Journal of the American Chemical Society* 140, no. 43 (2018): 14069–14072, https://doi.org/10.1021/jacs.8b09523.

15. M. Gobbi, S. Bonacchi, J. X. Lian, et al., "Collective Molecular Switching in Hybrid Superlattices for Light-Modulated Two-Dimensional Electronics," *Nature Communications* 9, no. 1 (2018): 2661, https://doi.org/10.1038/s41467-018-04932-z.

16. H. Qiu, Y. Zhao, Z. Liu, M. Herder, S. Hecht, and P. Samorì, "Modulating the Charge Transport in 2D Semiconductors via Energy-Level Phototuning," *Advanced Materials* 31, no. 39 (2019): 1903402, https://doi.org/10.1002/adma.201903402.

17. J. Li, J. Wierzbowski, Ö. Ceylan, et al., "Tuning the Optical Emission of MoS_2 Nanosheets Using Proximal Photoswitchable Azobenzene Molecules," *Applied Physics Letters* 105, no. 24 (2014): 241116.

18. M. Morant-Giner, J. M. Carbonell-Vilar, M. Viciano-Chumillas, A. Forment-Aliaga, J. Cano, and E. Coronado, "Functionalisation of MoS_2 2D Layers with Diarylethene Molecules," *Journal of Materials Chemistry C* 9, no. 33 (2021): 10975–10984, https://doi.org/10.1039/D1TC01133B.

19. S. Park, J. Ji, C. Cunningham, et al., "Photoswitchable Optoelectronic Properties of 2D $MoSe_2$/Diarylethene Hybrid Structures," *Scientific Reports* 14, no. 1 (2024): 7325, https://doi.org/10.1038/s41598-024-57479-z.

20. S. Park, J. Ji, S. Pillai, et al., "Layer-Number-Dependent Photoswitchability in 2D MoS_2-Diarylethene Hybrids," *Nanoscale* 17 (2025): 3152–3159.

21. A. Tamayo, W. Danowski, B. Han, Y. Jeong, and P. Samorì, "Light-Modulated Humidity Sensing in Spiropyran Functionalized MoS_2 Transistors," *Small* 22 (2024): 2404633.

22. M. S. Al Mamun, Y. Sainoo, T. Takaoka, et al., "Chemistry of the Photoisomerization and Thermal Reset of Nitro-spiropyran and Merocyanine Molecules on the Channel of the MoS_2 Field Effect Transistor," *Physical Chemistry Chemical Physics* 23, no. 48 (2021): 27273–27281.

23. H. Qiu, Z. Liu, Y. Yao, M. Herder, S. Hecht, and P. Samorì, "Simultaneous Optical Tuning of Hole and Electron Transport in Ambipolar WSe_2 Interfaced with a Bicomponent Photochromic Layer: from High-Mobility Transistors to Flexible Multilevel Memories," *Advanced Materials* 32, no. 11 (2020): 1907903, https://doi.org/10.1002/adma.201907903.

24. S. Park, J. Ji, J. Andreasson, J. H. You, and J. H. Choi, "Tunable Photodetectors Based on 2-D Hybrid Structures from Transition Metal Dichalcogenides and Photochromic Molecules," *IEEE Sensors Reviews* 2 (2025): 405–418, https://doi.org/10.1109/SR.2025.3595503.

25. K. L. Seyler, P. Rivera, H. Yu, et al., "Signatures of moiré-trapped Valley Excitons in $MoSe_2$/WSe_2 Heterobilayers," *Nature* 567, no. 7746 (2019): 66–70, https://doi.org/10.1038/s41586-019-0957-1.

26. H. Qiu, M. Herder, S. Hecht, and P. Samorì, "Ternary-Responsive Field-Effect Transistors and Multilevel Memories Based on Asymmetrically Functionalized Janus Few-Layer WSe_2," *Advanced Functional Materials* 31, no. 36 (2021): 2102721, https://doi.org/10.1002/adfm.202102721.

27. Y. Zhao, S. M. Gali, C. Wang, et al., "Molecular Functionalization of Chemically Active Defects in WSe_2 for Enhanced Opto-Electronics," *Advanced Functional Materials* 30, no. 45 (2020): 2005045, https://doi.org/10.1002/adfm.202005045.

28. P. K. Barman, P. Upadhyay, R. Rajarapu, S. K. Yadav, L. KVP, and P. K. Nayak, "Twist-Dependent Tuning of Excitonic Emissions in Bilayer WSe_2," *ACS Omega* 7, no. 7 (2022): 6412–6418, https://doi.org/10.1021/acsomega.1c07219.

29. J. Ji and J. H. Choi, "Layer-Number-Dependent Electronic and Optoelectronic Properties of 2D WSe_2 -Organic Hybrid Heterojunction," *Advanced Materials Interfaces* 6, no. 17 (2019): 1900637, https://doi.org/10.1002/admi.201900637.

30. H. Li, J. Wu, Z. Yin, and H. Zhang, "Preparation and Applications of Mechanically Exfoliated Single-Layer and Multilayer MoS_2 and WSe_2 Nanosheets," *Accounts of Chemical Research* 47, no. 4 (2014): 1067–1075, https://doi.org/10.1021/ar4002312.

31. Y. Shi, D. Sang, C. Li, et al., "Recent Progress of Optoelectronic Applications Based on 2D WSe_2 Nanomaterials and Heterostructures: A Review," *Journal of Materials Chemistry C* 13 (2025): 18555–18574, https://doi.org/10.1039/D5TC01545F.

32. R. Klajn, "Spiropyran-Based Dynamic Materials," *Chemical Society Reviews* 43, no. 1 (2014): 148–184, https://doi.org/10.1039/C3CS60181A.

33. L. Kortekaas and W. R. Browne, "The Evolution of Spiropyran: Fundamentals and Progress of an Extraordinarily Versatile Photochrome," *Chemical Society Reviews* 48, no. 12 (2019): 3406–3424, https://doi.org/10.1039/C9CS00203K.

34. H. Qiu, S. Ippolito, A. Galanti, Z. Liu, and P. Samorì, "Asymmetric Dressing of WSe_2 with (Macro) Molecular Switches: Fabrication of Quaternary-Responsive Transistors," *ACS Nano* 15, no. 6 (2021): 10668–10677, https://doi.org/10.1021/acsnano.1c03549.

35. H. Zhang, J. Ji, A. A. Gonzalez, and J. H. Choi, "Tailoring Photoelectrochemical Properties of Semiconducting Transition Metal Dichalcogenide Nanolayers with Porphyrin Functionalization," *Journal of Materials Chemistry C* 5, no. 43 (2017): 11233–11238, https://doi.org/10.1039/C7TC02861J.

36. Y. Wang, S. M. Gali, A. Slassi, D. Beljonne, and P. Samorì, "Collective Dipole-Dominated Doping of Monolayer MoS_2: Orientation and Magnitude Control via the Supramolecular Approach," *Advanced Functional Materials* 30, no. 36 (2020): 2002846, https://doi.org/10.1002/adfm.202002846.

37. D. M. Sim, M. Kim, S. Yim, et al., "Controlled Doping of Vacancy-Containing Few-Layer MoS_2 via Highly Stable Thiol-Based Molecular Chemisorption," *ACS Nano* 9, no. 12 (2015): 12115–12123, https://doi.org/10.1021/acsnano.5b05173.

38. H. Zhang, J. Choi, A. Ramani, et al., "Engineering Chemically Exfoliated Large-Area Two-Dimensional MoS_2 Nanolayers with Porphyrins for Improved Light Harvesting," *Chemphyschem* 17, no. 18 (2016): 2854–2862, https://doi.org/10.1002/cphc.201600511.

39. Y. Pan, M. Rahaman, L. He, et al., "Exciton Tuning in Monolayer WSe_2 via Substrate Induced Electron Doping," *Nanoscale Advances* 4, no. 23 (2022): 5102–5108, https://doi.org/10.1039/D2NA00495J.

40. A.-R. Jang, E. K. Jeon, D. Kang, et al., "Reversibly Light-Modulated Dirac Point of Graphene Functionalized with Spiropyran," *ACS Nano* 6, no. 10 (2012): 9207–9213, https://doi.org/10.1021/nn303539y.

41. J. S. Eo, J. Shin, S. Yang, et al., "Tailoring the Interfacial Band Offset by the Molecular Dipole Orientation for a Molecular Heterojunction Selector," *Advanced Science* 8, no. 21 (2021): 2101390, https://doi.org/10.1002/advs.202101390.

42. A. Allain and A. Kis, "Electron and Hole Mobilities in Single-Layer WSe_2," *ACS Nano* 8, no. 7 (2014): 7180–7185, https://doi.org/10.1021/nn5021538.

43. A. Riemann, L. Rankin, and D. Henry, "Atomic Charge Dependency of Spiropyran/Merocyanine Adsorption as a Precursor to Surface Isomerization Reactions," *ACS Omega* 9, no. 1 (2023): 798–810, https://doi.org/10.1021/acsomega.3c06712.

44. Y. Wang, D. Iglesias, S. M. Gali, D. Beljonne, and P. Samorì, "Light-Programmable Logic-in-memory in 2D Semiconductors Enabled by Supramolecular Functionalization: Photoresponsive Collective Effect of Aligned Molecular Dipoles," *ACS Nano* 15, no. 8 (2021): 13732–13741, https://doi.org/10.1021/acsnano.1c05167.

45. E. Margapoti, J. Li, Ö. Ceylan, et al., "A 2D Semiconductor–Self-Assembled Monolayer Photoswitchable Diode," *Advanced Materials* 27 (2015): 1426–1431, https://doi.org/10.1002/adma.201405110.

46. B. Rybtchinski, "Adaptive Supramolecular Nanomaterials Based on Strong Noncovalent Interactions," *ACS Nano* 5, no. 9 (2011): 6791–6818, https://doi.org/10.1021/nn2025397.

47. F. J. Costa, T. G. Brito, I. D. Barcelos, and L. F. Zagonel, "Impacts of Dielectric Screening on the Luminescence of Monolayer WSe_2," *Nanotechnology* 34, no. 38 (2023): 385703, https://doi.org/10.1088/1361-6528/acda3b.

48. R. Itzhak, N. Suleymanov, B. Minkovich, et al., "Exciton Manipulation via Dielectric Environment Engineering in 2D Semiconductors," *ACS Applied Optical Materials* 3, no. 6 (2025): 1330–1338, https://doi.org/10.1021/acsaom.5c00105.

49. A. Slassi, R. Moukaouine, J. Cornil, and A. Pershin, "Controlling Charge Carrier Lifetime in Defective WSe_2 Monolayer through Interface Engineering: A Time-Domain Ab Initio Study," *The Journal of Physical Chemistry Letters* 16, no. 8 (2025): 1931–1938, https://doi.org/10.1021/acs.jpclett.4c03723.

50. W. Zhao, Z. Ghorannevis, L. Chu, et al., "Evolution of Electronic Structure in Atomically Thin Sheets of WS_2 and WSe_2," *ACS Nano* 7, no. 1 (2013): 791–797, https://doi.org/10.1021/nn305275h.

51. B. Zhu, X. Chen, and X. Cui, "Exciton Binding Energy of Monolayer WS_2," *Scientific Reports* 5, no. 1 (2015): 9218, https://doi.org/10.1038/srep09218.

52. A. Hanbicki, M. Currie, G. Kioseoglou, A. Friedman, and B. Jonker, "Measurement of High Exciton Binding Energy in the Monolayer Transition-metal Dichalcogenides WS_2 and WSe_2," *Solid State Communications* 203 (2015): 16–20.

53. A. Chernikov, T. C. Berkelbach, H. M. Hill, et al., "Exciton Binding Energy and Nonhydrogenic Rydberg Series in Monolayer WS_2," *Physical Review Letters* 113, no. 7 (2014): 076802, https://doi.org/10.1103/PhysRevLett.113.076802.

54. A. Raja, A. Chaves, J. Yu, et al., "Coulomb Engineering of the Bandgap and Excitons in Two-Dimensional Materials," *Nature Communications* 8, no. 1 (2017): 15251, https://doi.org/10.1038/ncomms15251.

55. A. Chernikov, A. M. Van Der Zande, H. M. Hill, et al., "Electrical Tuning of Exciton Binding Energies in Monolayer WS_2," *Physical Review*

Letters 115, no. 12 (2015): 126802, https://doi.org/10.1103/PhysRevLett.115.126802.

56. Z. Li, F. Rashvand, H. Bretscher, et al., "Understanding the Photoluminescence Quenching of Liquid Exfoliated WS_2 Monolayers," *The Journal of Physical Chemistry C* 126, no. 51 (2022): 21681–21688, https://doi.org/10.1021/acs.jpcc.2c05284.

57. Z. Morales, N. Rühl, et al., "Strong Coupling of Monolayer WS_2 Excitons and Surface Plasmon Polaritons in a Planar Ag/WS_2 Hybrid Structure," *Physical Review B* 108, no. 16 (2023): 165426, https://doi.org/10.1103/PhysRevB.108.165426.

58. C. H. Stansbury, M. I. B. Utama, C. G. Fatuzzo, et al., "Visualizing Electron Localization of WS_2/WSe_2 Moiré Superlattices in Momentum Space," *Science Advances* 7, no. 37 (2021): abf4387, https://doi.org/10.1126/sciadv.abf4387.

59. Q. Alam, S. Sardar, H. Din, et al., "A First Principles Study of a van der Waals Heterostructure Based on MS^2 (M = Mo, W) and Janus CrSSe Monolayers," *Nanoscale Advances* 4, no. 17 (2022): 3557–3565, https://doi.org/10.1039/D2NA00298A.

60. J. Sun, Y. Choi, Y. J. Choi, et al., "2D–Organic Hybrid Heterostructures for Optoelectronic Applications," *Advanced Materials* 31, no. 34 (2019): 1803831, https://doi.org/10.1002/adma.201803831.

61. B. Han and P. Samorì, "Engineering the Interfacing of Molecules with 2D Transition Metal Dichalcogenides: Enhanced Multifunctional Electronics," *Accounts of Chemical Research* 57, no. 17 (2024): 2532–2545, https://doi.org/10.1021/acs.accounts.4c00338.

62. K. S. Novoselov, A. K. Geim, S. V. Morozov, et al., "Electric Field Effect in Atomically Thin Carbon Films," *Science* 306, no. 5696 (2004): 666–669, https://doi.org/10.1126/science.1102896.

63. J. Ji and J. H. Choi, "Understanding the Effects of Dielectric Property, Separation Distance, and Band Alignment on Interlayer Excitons in 2D Hybrid MoS_2/WSe_2 Heterostructures," *ACS Applied Electronic Materials* 3, no. 7 (2021): 3052–3059, https://doi.org/10.1021/acsaelm.1c00282.

64. S. Park, J. Ha, M. F. Khan, et al., "Pronounced Optoelectronic Effect in n–n ReS_2 Homostructure," *ACS Applied Electronic Materials* 4, no. 9 (2022): 4306–4315, https://doi.org/10.1021/acsaelm.2c00567.

65. X. Cui, Q. Ruan, X. Zhuo, et al., "Photothermal Nanomaterials: a Powerful Light-to-Heat Converter," *Chemical Reviews* 123, no. 11 (2023): 6891–6952, https://doi.org/10.1021/acs.chemrev.3c00159.

66. J. Ji, C. M. Delehey, D. N. Houpt, M. K. Heighway, T. Lee, and J. H. Choi, "Selective Chemical Modulation of Interlayer Excitons in Atomically Thin Heterostructures," *Nano Letters* 20, no. 4 (2020): 2500–2506, https://doi.org/10.1021/acs.nanolett.9b05254.

67. G. Kresse and J. Hafner, "Ab Initio Molecular Dynamics for Liquid Metals," *Physical Review B* 47, no. 1 (1993): 558–561, https://doi.org/10.1103/PhysRevB.47.558.

68. G. Kresse and J. Furthmüller, "Efficiency of Ab-Initio Total Energy Calculations for Metals and Semiconductors Using a Plane-Wave Basis Set," *Computational Materials Science* 6, no. 1 (1996): 15–50, https://doi.org/10.1016/0927-0256(96)00008-0.

69. G. Kresse and J. Furthmüller, "Efficient Iterative Schemes for Ab Initio Total-Energy Calculations Using a Plane-Wave Basis Set," *Physical Review B* 54, no. 16 (1996): 11169–11186, https://doi.org/10.1103/PhysRevB.54.11169.

70. J. P. Perdew, K. Burke, and M. Ernzerhof, "Generalized Gradient Approximation Made Simple," *Physical Review Letters* 77, no. 18 (1996): 3865–3868, https://doi.org/10.1103/PhysRevLett.77.3865.

71. S. Grimme, "Semiempirical GGA-Type Density Functional Constructed with a Long-Range Dispersion Correction," *Journal of Computational Chemistry* 27, no. 15 (2006): 1787–1799, https://doi.org/10.1002/jcc.20495.

Supporting Information

Additional supporting information can be found online in the Supporting Information section.

Supporting File: admt71071-sup-0001-SuppMat.pdf.